Journal of Power Sources 216 (2012) 425–433

Contents lists available at SciVerse ScienceDirect

Journal of Power Sources

journal homepage: www.elsevier.com/locate/jpowsour

Microstructure and supercapacitive properties of buserite-type manganese oxide with a large basal spacing

Zhenjie Sun [a], Dong Shu [a,b,d,*], Hongyu Chen [a,b,d], Chun He [c,**], Shaoqing Tang [a], Jie Zhang [a]

[a] School of Chemistry and Environment, South China Normal University, Guangzhou 510006, PR China
[b] Base of Production, Education & Research on Energy Storage and Power Battery of Guangdong Higher Education Institutes, Guangzhou 510006, PR China
[c] School of Environmental Science and Engineering, Sun Yat-sen University, Guangzhou 510275, PR China
[d] Key Laboratory of Electrochemical Technology on Energy Storage and Power Generation of Guangdong Higher Education Institutes, South China Normal University, Guangzhou 510006, PR China

HIGHLIGHTS

- Mg–buserite with a large basal spacing of 10 Å was successfully synthesized.
- Mg^{2+} and two sheets of H_2O molecules occupy the interlayer region of Mg–buserite.
- The maximum specific capacitance of Mg–buserite is 164 F g^{-1} at 1 mV s^{-1}.
- The specific capacitance of Mg–buserite decreased only 6% after 22,000 cycles.
- The superior capacitive behaviors are attributed to the large basal spacing.

ARTICLE INFO

Article history:
Received 11 January 2012
Received in revised form
14 May 2012
Accepted 28 May 2012
Available online 4 June 2012

Keywords:
Manganese oxide
Buserite
Large basal spacing
Supercapacitor
Cycle stability

ABSTRACT

A hydration-layered structure of buserite-type manganese oxide (Mg–buserite) was successfully synthesized by an ion exchange method. The as-prepared Mg–buserite possesses a large basal spacing of 10 Å, and contains Mg^{2+} ions and two sheets of water molecules in the interlayer region. The supercapacitive behaviors of Mg–buserite were systematically investigated by cyclic voltammetry (CV), galvanostatic charge–discharge (CD) experiments and electrochemical impedance spectroscopy (EIS). The results showed that the specific capacitance of the Mg–buserite electrode sharply increased during the initial 500 cycles and reached a maximum of 164 F g^{-1} at approximately the 500th cycle at a scan rate of 1 mV s^{-1}, and then it remained an almost constant value and decreased slightly upon prolonged cycling. After 22,000 cycles, the specific capacitance decreased by approximately 6% of the maximum specific capacitance. The superior capacitive behavior and excellent cycling stability of the as-prepared Mg–buserite are attributed to the large basal spacing, which can accommodate a larger amount of electrolyte cations and provide more favorable pathways for electrolyte cations intercalation and deintercalation. The experimental results demonstrate that Mg–buserite is a promising candidate as an electrode material for supercapacitors.

1. Introduction

Currently, supercapacitors have gained enormous attention owing to their higher energy density compared with conventional electrical double-layer capacitors and greater power density and longer cycle life than secondary batteries [1,2]. Accordingly, they have been employed in a wide range of applications, such as in portable electronics, memory back-up systems and hybrid electric vehicles [3,4].

Most researchers in this field have focused on the development of new electrode materials with improved electrochemical properties [5]. Generally, the electrode materials used in supercapacitors mainly include carbon materials, transition metal oxides and conducting polymers [6]. Among all of the potential materials investigated for supercapacitor electrodes over the years, amorphous hydrous ruthenium oxide ($RuO_2 \cdot xH_2O$) exhibits much higher specific capacitance (760 F g^{-1}) than conventional carbon

* Corresponding author. School of Chemistry and Environment, South China Normal University, Guangzhou 510006, PR China. Tel.: +86 20 39310212; fax: +86 20 39310187.
** Corresponding author. Tel./fax: +86 20 39332690.
E-mail addresses: dshu@scnu.edu.cn (D. Shu), hechun@mail.sysu.edu.cn (C. He).

0378-7753/$ – see front matter © 2012 Elsevier B.V. All rights reserved.
http://dx.doi.org/10.1016/j.jpowsour.2012.05.087

materials and better electrochemical stability than conducting polymer materials [7]. However, the high cost and toxic nature of hydrous ruthenium oxide greatly limit its commercial implementation. Manganese oxides have been considered as one of the most promising electrode materials for supercapacitor's applications in replacing ruthenium oxide with respect to their natural abundance, low cost, environmentally friendly nature, wide voltage windows and high specific capacitance [8]. A literature survey reveals that many efforts have been paid to layered structure manganese oxides most recently; especially birnessite-type manganese oxide has been wildly used as an electrode material in lithium rechargeable batteries and supercapacitors. Athouel et al. [9] reported the specific capacitance of 145 F g^{-1} at a scan rate of 2 mV s^{-1} for layered structure Mg-doped sodium birnessite-type MnO_2. Matsuo et al. [10] prepared birnessite-type manganese oxide containing a small amount of vanadium, and 83% of the initial discharge capacity was maintained only after 10 cycles. In the works of Ogata et al. [11], the potassium birnessites were synthesized by a thermal decomposition reaction and the capacity retention was approximately 80% after 20 cycles. As reported by Komaba et al. [12], the nano-structured birnessite was prepared by successive potential cycles in a mild aqueous electrolyte, and applied as positive electrode for supercapacitors. The loss of capacitance was calculated to be approximately 16% of the initial after 1800 cycles. Notably, there is a serious drawback to the birnessite-type manganese oxide used as an electrode material, that is, the poor cycling stability, which still limits its potential applications.

Na–birnessite is a typical birnessite-type manganese oxide, it possesses a two-dimensional layered structure which forms MnO_2 sheets of edge-sharing MnO_6 octahedra assembled in layers and one sheet of water molecules and Na^+ ions in the interlayer region, and the basal spacing is typically 7.1 Å (the interlayer distance plus the thickness of the host manganese oxide layers equals the basal spacing while the interlayer spacing does not contain the thickness of the host manganese oxide layers) [13,14]. When Na^+ ions are replaced by Mg^{2+} ions, Mg–buserite is obtained. Mg–buserite retains the layered structure of Na–birnessite but has an enlarged basal spacing of 10 Å due to the introduction of an extra sheet of interlayer water molecules [14–19]. Fig. 1 presents the crystal structure of Na–birnessite and Mg–buserite. The large basal spacing and two sheets of interlayer water molecules of Mg–buserite would provide more favorable pathways for electrolyte cations intercalation and deintercalation as compared with Na–birnessite. In addition, the large basal spacing can accommodate a large amount of electrolyte cations, which would provide more pseudocapacitive contribution. Furthermore, because the hydrated Mg^{2+} ion is larger than the hydrated Na^+ ion [9], the intercalation and deintercalation of Na^+ ions from the electrolyte into the interlayer of Mg–buserite would not induce the significant structural or microstructural changes, leading to excellent cycling stability. The above analysis results reveal that Mg–buserite would be a promising candidate as an electrode material for supercapacitors. However, to the best of our knowledge, up to now there have been very few papers reported on the application of Mg–buserite as an electrode material for supercapacitors. In the present study, Mg–buserite which possesses large basal spacing and two sheets of interlayer water molecules was synthesized and employed as an active electrode material for a supercapacitor. The supercapacitive properties of the Mg–buserite electrode were systematically investigated in 0.1 M Na_2SO_4 electrolyte. The results show that the as-prepared Mg–buserite exhibits high pseudocapacitance and excellent cycling stability.

2. Experimental

2.1. Material synthesis

Mg–buserite was synthesized following a procedure similar to the previous report by Ching et al. [15]. At room temperature, 3.4 g of $MnSO_4 \cdot H_2O$ powder was dissolved in 20 mL of distilled water, and then 30 mL of NaOH (6 M) aqueous solution was added drop by drop into the solution under vigorous stirring, obtaining a light brown slurry of $Mn(OH)_2$. After stirring for approximately 1 h, 0.7 g of $MgSO_4 \cdot 7H_2O$ and 3.2 g of $(NH_4)_2S_2O_8$ granular mixture were very slowly added into the slurry, and an olive–green slurry of Mg-doped Na–birnessite was obtained. The resultant system was stirred for 2 h and then filtered and repeatedly washed with distilled water. Mg–buserite was prepared by dispersing Mg-doped Na–birnessite in 300 mL of 1 M of $MgCl_2$ solution and stirring for 3 days at room temperature. The resulting mixture was filtered, washed with distilled water, and dried at 60 °C for 24 h under vacuum, and a brown Mg–buserite powder was obtained.

2.2. Material characterization

The crystallographic structure of the as-prepared powder was characterized by powder X-ray diffraction (XRD) using a D/MAX 2200 VPC X-ray generator in which Cu Kα used as the radiation source. Thermogravimetric analysis (TGA) for the sample was carried out in a nitrogen atmosphere from ambient to 800 °C at a heating rate of 10 °C min^{-1} by a STA409PC Diamond TG-DTA thermal analyzer. The pore size distribution and specific surface area of the sample were analyzed using a surface area analyzer (ASAP-2020, Micromeritics, America), and they were calculated by the Barrett–Joyner–Halenda (BJH) method and the Brunauer–Emmett–Teller (BET) equation, respectively. The morphology and microstructure of the sample were

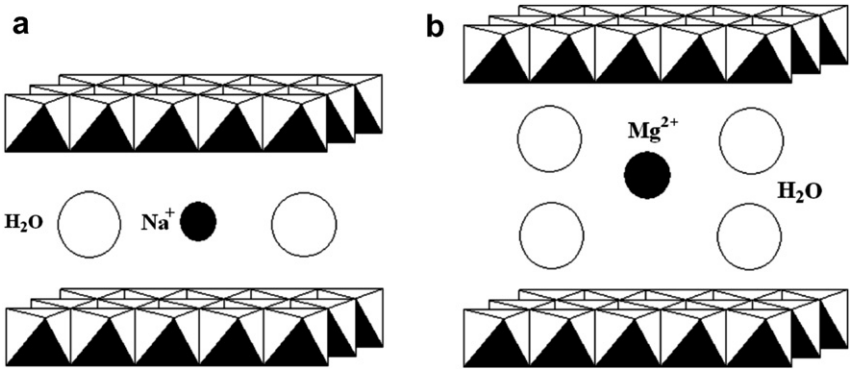

Fig. 1. The microstructure of (a) Na–birnessite and (b) Mg–buserite.

obtained from a ZEISS Ultra-55 scanning electron microscope equipped with an energy dispersive X-ray (EDX) spectrometer for the semiquantitative analysis. X-ray photoelectron spectroscopy (XPS) measurements for the sample were performed with an ESCALAB 250 X-ray photoelectron spectrometer. Fourier transformation infrared (FT-IR) spectra were recorded using a Fourier transform IR spectrometer (IR-prestige21, Shimadzu Co., Japan) by making pellets with KBr.

2.3. Electrochemical measurements

The working electrode of supercapacitors was prepared by mixing 85 wt.% of the as-prepared Mg–buserite powder as active material, 10 wt.% of acetylene black and 5 wt.% of polyvinylidene fluoride (PVDF). A slurry of the mixture was made using *N*-methyl-2-pyrrolidone (NMP) as a solvent, then the resulting mixture was coated onto a stainless steel grid with an apparent area of 1×1 cm, and dried under vacuum at 60 °C for 12 h. The electrochemical measurements were carried out using a conventional three-electrode system in which the as-prepared Mg–buserite electrode is the working electrode, saturated calomel electrode (SCE) is the reference electrode and graphite electrode is the counter electrode. All the electrochemical measurements were carried out in 0.1 M Na_2SO_4 electrolyte. Cyclic voltammetry (CV) and galvanostatic charge–discharge (CD) experiments were measured by a CHI 660A electrochemical working station. CV curves were recorded in the potential range from −0.1 to 0.9 V at various scan rates from 1 to 100 mV s^{-1}, and the cycling behavior of the Mg–buserite electrode was characterized up to 22,000 cycles. CD measurements were also carried out in the potential range from −0.1 to 0.9 V at different current densities of 0.2, 0.5, 1, 2, 3 and 4Ag^{-1} A g^{-1}. Electrochemical impedance spectroscopy (EIS) tests were measured at different potentials using the frequency range from 10^{-2} Hz to 100 kHz by an Autolab PGSTAT30.

3. Results and discussion

3.1. Characterization of materials

The as-prepared Mg–buserite powder was characterized by XRD and compared with Mg-doped Na–birnessite powder; the XRD data are presented in Fig. 2. Fig. 2a shows that two strong and sharp diffraction peaks appear at $2\theta = 9.1°$ and 18.3°, which indicate good crystallinity of the sample. Besides these two main diffraction peaks, another one weak diffraction peak could be observed at 27.5°. All of the diffraction peaks can be indexed as Mg–buserite with a basal spacing of 10 Å (JCPDS 32-1128), and in agreement with the previous studies of Mg–buserite [15–17]. Fig. 2c shows the XRD pattern of the as-prepared Mg-doped Na–birnessite. The diffraction peaks at $2\theta = 12.4°$ and 25.1° are respectively assigned as the (0 0 1) and (0 0 2) reflections of birnessite-type manganese oxide (JCPDS 23-1046). The XRD results reveal different structural characteristics for the two samples, and further demonstrate the expected increase in the basal spacing from 7.1 Å in Mg-doped Na–birnessite to 10 Å in Mg–buserite.

The Na/Mn and Mg/Mn atomic ratios of Mg-doped Na–birnessite and Mg–buserite determined from EDX analyses are shown in Fig. 3. The Na/Mn and Mg/Mn atomic ratios of Mg-doped Na–birnessite are 0.19 and 0.11, respectively. After ion exchange reactions, the higher Mg/Mn atomic ratio and much lower Na/Mn atomic ratio for Mg–buserite indicate that Na^+ ions were almost completely exchanged by Mg^{2+} ions and Mg–buserite was synthesized. The slight amount of Na^+ ions in Mg–buserite matrix is mainly due to the residual Na^+ ions that remain after repeated cleaning during synthesis.

Fig. 4 compares the TGA curves of Mg–buserite and Mg-doped Na–birnessite. The total weight losses are 23.4 wt.% and 19.6 wt.% for Mg–buserite and Mg-doped Na–birnessite, respectively. The main difference in weight loss occurs in the range of temperature from 150 to 350 °C. It can be clearly observed that this process is more important for Mg–buserite (about 10.1 wt.%) than Mg-doped Na–birnessite (6.8 wt.%). In this range of temperature, the weight loss generally ascribes to the dehydration of the interlayer H_2O molecules [20]. The result suggests that the amount of interlayer water molecules of Mg–buserite is larger than that of Mg-doped Na–birnessite, which is in agreement with one and two sheets of interlayer water molecules in Mg-doped Na–birnessite and Mg–buserite, respectively. According to the literature [2,21], the pseudocapacitance of the oxide materials depends on the water content. With increasing the water content, the transportation of active ionic species increases.

As the temperature increases from 520 °C to around 600 °C, the abrupt weight loss of the two samples is probably attributed to the reduction of manganese from tetravalent to trivalent accompanied by the generated oxygen releases from the manganese oxides, resulting in the transformation of the samples into Mn_2O_3 [22,23].

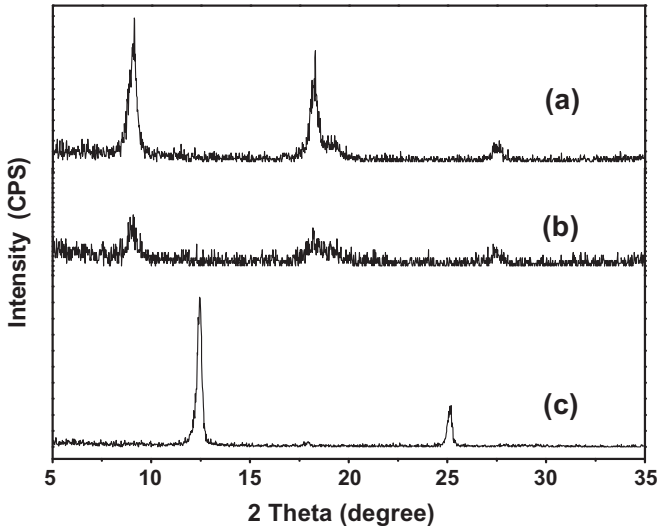

Fig. 2. (a) XRD patterns of Mg–buserite before cycle and (b) after 500 cycles, (c) XRD patterns of Mg-doped Na–birnessite.

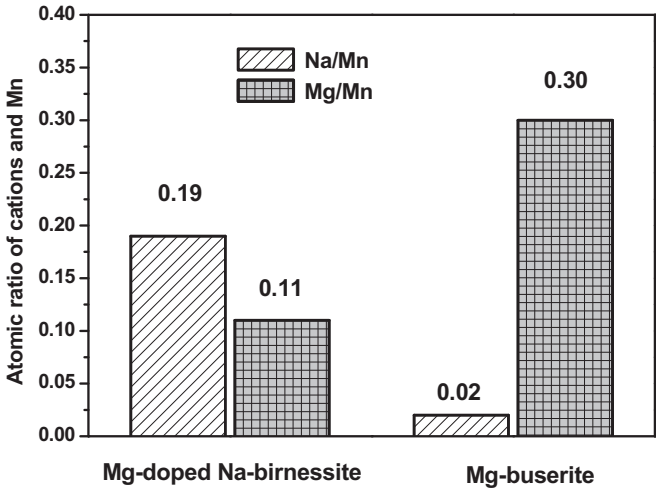

Fig. 3. The relative content of Na^+ and Mg^{2+} in two MnO_2 powders: Mg–buserite and Mg-doped Na–birnessite obtained from EDX studies.

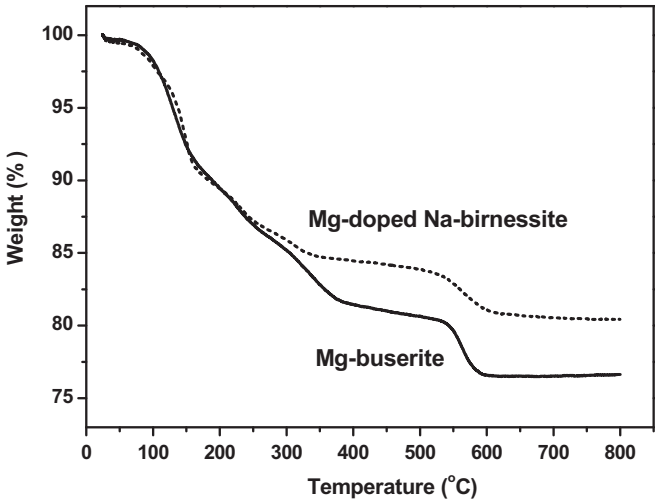

Fig. 4. TGA curves of two MnO_2 powders: Mg–buserite and Mg-doped Na–birnessite.

The results of the above XRD, EDX and TGA analysis demonstrate that Mg–buserite was successfully synthesized. The as-prepared Mg–buserite retains the layered structure of Na–birnessite but has an enlarged basal spacing of 10 Å, which forms MnO_2 sheets of edge-sharing MnO_6 octahedra assembled in layers and Mg^{2+} ions and two sheets of water molecules in the interlayer.

Nitrogen adsorption–desorption experiments were performed to determine the specific surface area and the pore size distribution of Mg–buserite, and the nitrogen adsorption–desorption isotherms and BJH pore size distribution plot (inset) are shown in Fig. 5. N_2 adsorption and desorption curves of Mg–buserite exhibit a small hysteresis loop between the adsorption and desorption branches, which classified as type IV according to the International Union of Pure and Applied Chemistry (IUPAC), indicating the presence of mesopores in Mg–buserite [24]. However, the fraction of mesopores is not so large because the hysteresis loop is not so clear. The inset of Fig. 5 shows the pore size distribution of Mg–buserite. The average pore diameter of Mg–buserite is around 14.4 nm, and the major pore size distribution peaks center at 1.9, 3.8 and 30.9 nm, which confirms the presence of mesopores in Mg–buserite. The measured BET surface area and corresponding pore volume of Mg–buserite are found to be 36.80 $m^2\ g^{-1}$ and 0.13 $cm^3\ g^{-1}$, respectively, which are greater than the BET surface area of 31.65 $m^2\ g^{-1}$ and pore volume of 0.09 $cm^3\ g^{-1}$ for the as-prepared Mg-doped Na–birnessite. The relatively higher BET surface area of Mg–buserite can provide more redox active sites, which would lead to excellent electrochemical capacitive properties [25].

The surface morphology of the as-synthesized Mg–buserite was examined by SEM, and the SEM photograph is displayed in Fig. 6. The particles show a thin plate-like morphology. The fragmented platelets are irregular in shape and do not aggregate together. The sizes of the platelets are mainly in the range of 200–1000 nm. The thickness of the different platelets is rather uniform, which is estimated by the cross-sectional SEM image to be approximately 50 nm. The electrolyte would easily soak into the thin plate-like Mg–buserite, which facilitates the diffusion of electrolyte cations into the bulk of the Mg–buserite electrode.

XPS was employed to study the surface electronic states of Mg–buserite, and the Mn 2p, Mg 1s and O 1s XPS spectra of Mg–buserite are displayed in Fig. 7a, b and c, respectively. The Mn 2p spectrum of Mg–buserite was analyzed by curve fitting, and the Mn $2P_{3/2}$ and Mn $2p_{1/2}$ signals were deconvoluted into three separate peaks. The peaks at binding energies of 642.6 eV and 654.0 eV are assigned to Mn $2p_{3/2}$ and Mn $2p_{1/2}$, respectively, indicating that Mn is present in the chemical state of Mn^{4+} [26]. The third peak appears at a binding energy of 641.3 eV, which corresponds to Mn $2p_{3/2}$. Generally, the lower applied potential led to the lower binding energy of the Mn $2p_{3/2}$ electron, suggesting that manganese is in a lower chemical state. Thus, the binding energy of 641.3 eV for Mn $2P_{3/2}$ indicates the presence of the Mn^{3+} chemical state in Mg–buserite [27]. The results indicate that a mixture of tetravalent and trivalent manganese exist in the as-prepared Mg–buserite. Fig. 7b depicts the XPS spectrum of the Mg 1s orbital of Mg–buserite. From the shape of the Mg 1s spectrum, it can be concluded that more than one chemical environment of the Mg atoms exist in the as-prepared Mg–buserite. The Mg 1s spectrum was fitted with two peaks, while the framework incorporation of Mg^{2+} ions for structural stability have a binding energy of 1303.7 eV and the interlayer Mg^{2+} ions between the manganese oxide sheets to support the layer structure have a binding energy of 1303.1 eV. The O 1s spectrum of the Mg–buserite is shown in Fig. 7c. The spectrum can be deconvoluted into two sharp peaks and one broad peak, which correspond to three different oxygen-containing species: the anhydrous manganese oxide (Mn–O–Mn) at 530.0 eV, the manganese hydroxide

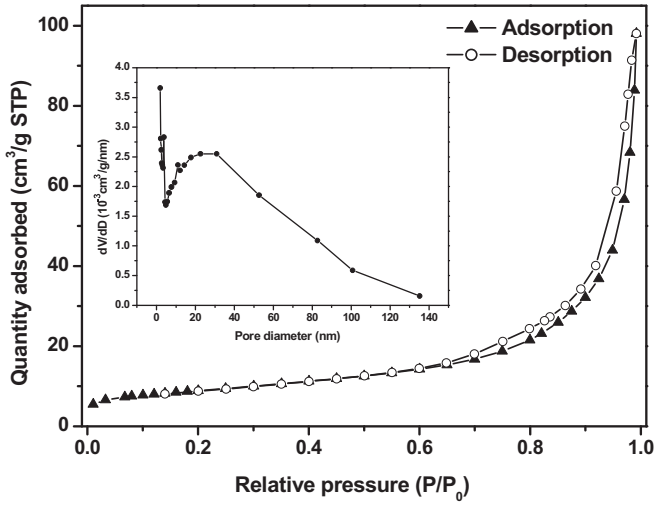

Fig. 5. Nitrogen adsorption–desorption isotherms and BJH pore-size distribution plots of Mg–buserite.

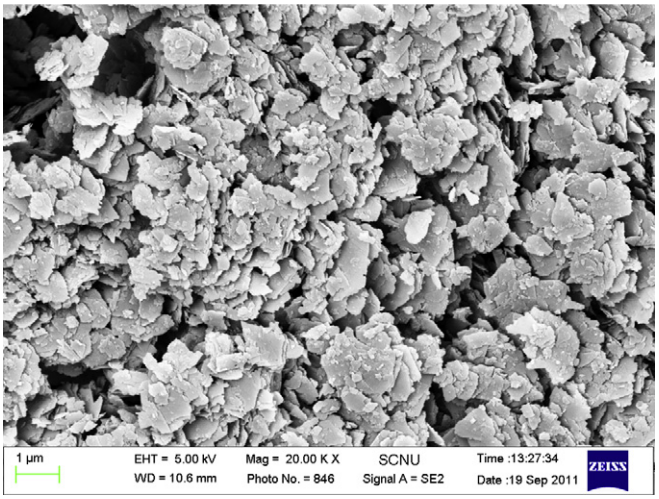

Fig. 6. SEM images of the as-prepared Mg–buserite.

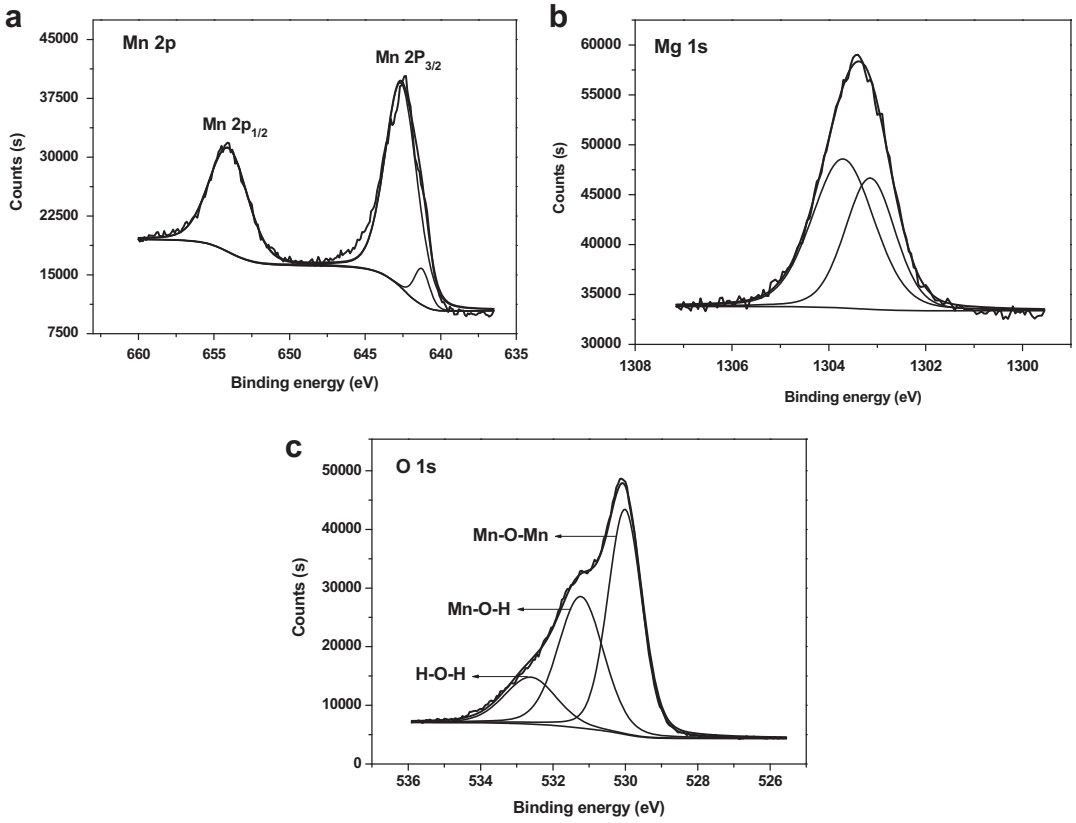

Fig. 7. XPS spectra of Mg–buserite: (a) Mn 2p peak, (b) Mg 1s peak and (c) O 1s peak.

(Mn–O–H) at 531.2 eV and the water molecule (H–O–H) at 532.6 eV, which are in good agreement with literature values of 529.3–530.3 eV for Mn–O–Mn, 530.5–531.5 eV for Mn–O–H and 531.8–532.8 eV for H–O–H [28,29]. In general, the peak area which is measured as a percentage of the total peak area can be used to estimate the relative amount of the corresponding part in the sample. The XPS data indicate that the as-prepared Mg–buserite contains a large amount of hydroxide and structure water. According to the literature [30], a certain amount of hydroxide and structure water content can enhance the diffusion of electrolyte cations in the electrode material, which is beneficial to the electrochemical performance of the material.

3.2. Electrochemical properties

The as-prepared Mg–buserite was employed as an active electrode material for a supercapacitor and its supercapacitive properties were first studied by the CV technique. Fig. 8a shows the first-cycle CV curve of the Mg–buserite electrode at a scan rate of 5 mV s^{-1} in 0.1 M Na_2SO_4 electrolyte within the potential range of −0.1 to 0.9 V versus SCE. Two broad redox peaks are observed at 0.64 and 0.38 V in the CV curve, which attributed to the faradaic charge-transfer processes [31]. The specific capacitance can be calculated from the CV curve according to the following equation:

$$SC\ (CV) = Q/m\Delta V \quad (1)$$

where SC is the specific capacitance (F g^{-1}), Q the cathodic charge (C), m the mass of active material in the working electrode (g) and ΔV is the width of the potential window (V). The specific capacitance obtained from the first-cycle CV curve is found to be 89 F g^{-1}.

During the CV test, it is interesting to find that a rapid increase of the specific capacitance is observed during the cycling. Such an improvement of the specific capacitance upon cycling has already been reported for MnO_2 materials [8,32,33]. After 500 cycles, the Mg–buserite electrode shows the best electrochemical capacitive properties. Thus, further experiments were performed on the Mg–buserite electrode after 500 cycles.

Fig. 8b shows the 500th-cycle CV curve at a scan rate of 5 mV s^{-1}. Three redox peaks are observed in the CV curve: the anodic current peak is located at 0.58 V while cathodic peaks located at approximately 0.47 and 0.41 V. The redox peaks can be regarded as the reversible intercalation/deintercalation of Na^+ ions in the electrode with charge transfer process at the electrode/electrolyte interface,

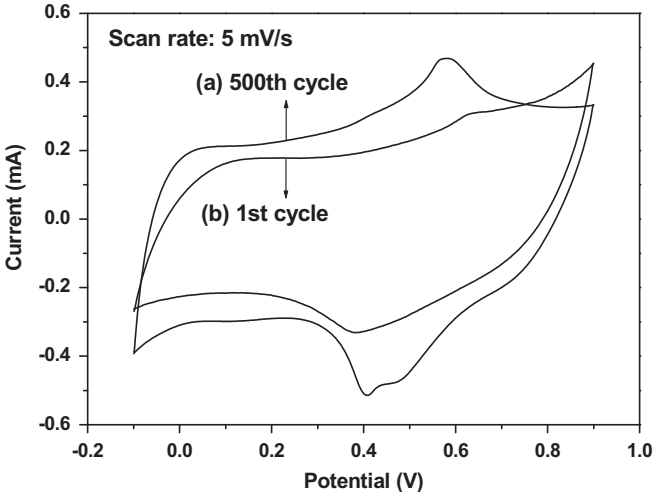

Fig. 8. The first cycle and 500th cycle cyclic voltammograms for the Mg–buserite electrode recorded at a scan rate of 5 mV s^{-1}.

which provide an additional pseudocapacitive contribution [22]. A comparison of Fig. 8a and b reveals that the anodic and cathodic currents clearly increased over the whole potential range after 500 cycles, indicating an enhancement of the specific capacitance [34]. The specific capacitance obtained from the 500th-cycle CV curve at a scan rate 5 mV s^{-1} is 134 F g^{-1}.

Electrochemical properties of the Mg–buserite electrode after 500 cycles were further studied by the CV technique in 0.1 M Na_2SO_4 electrolyte at various scan rates, and the corresponding CV curves are shown in Fig. 9a. It can be observed that the CV curves of the sample show typical pseudocapacitive behavior at low scan rates, but the redox peaks weaken and disappear with an increase in the scan rate. The specific capacitance values calculated from the CV curves are found to be 164, 134, 117, 101 and 73 F g^{-1} at scan rates of 1, 5, 10, 20 and 50 mV s^{-1}, respectively. The specific capacitance values quickly decrease as the scan rate increases. The significant dependence of the specific capacitance upon the scan rate is due to the fact that pseudocapacitance is the main contribution to the observed overall capacitance. At low scan rates, the diffusion of Na^+ ions from the electrolyte can gain access to almost all available pores of the electrode, which lead to nearly full utilization of the active sites of the electrode material, resulting in almost ideal pseudocapacitive behavior. However, increasing the scan rate has a direct impact on the diffusion of Na^+ ions from the electrolyte into the bulk of Mg–buserite electrode; Na^+ ions can only reach the outer surface of the electrode. Thus, the effective intercalation between the electrolyte cations and the electrode is greatly reduced, which directly lead to the rapid decrease of the specific capacitance [25,35].

To get more information on the electrochemical behavior of the as-synthesized Mg–buserite, further galvanostatic charge–discharge measurements were focused on the Mg–buserite electrode after 500 cycles, and the charge–discharge curves at different current densities are shown in Fig. 9b. The charge–discharge curves show a slight curvature characteristic, implying the pseudocapacitive contribution along with the double layer contribution [36]. This is consistent with the above CV result, where three redox current peaks were observed in the CV curve. The specific capacitance was calculated from the charge discharge curves using the following equation:

$$\mathrm{SC\ (CD)} = I\Delta t/m\Delta V \qquad (2)$$

where SC is the specific capacitance (F g^{-1}), I the charge or discharge current (A), Δt the discharge time (s), m the mass of active material in the working electrode (g) and ΔV is the width of the potential window (V). The average specific capacitances are 173, 144, 126 and 104 F g^{-1} at the current densities of 0.2, 0.5, 1 and 2 A g^{-1}, respectively.

To understand the relationship between the specific capacitance values calculated from CV experiments and those obtained by CD tests, the scan rate in the CV experiments and the discharge time in the CD tests were converted into a discharge rate. Fig. 9c shows the specific capacitance values (calculated from the CV and CD tests) of the Mg–buserite electrode after 500 cycles versus the discharge rate. It can be clearly observed that the specific capacitance values calculated from the CD tests are close to but slightly larger than those obtained by the CV experiments at the same discharge rate, and the specific capacitance values calculated from the CV and CD tests show the same tendency of decreasing with the increase of the discharge rate.

XRD analysis was used to investigate the possible structural changes of Mg–buserite after 500 cycles. The resulting XRD pattern is shown in Fig. 2b. After 500 cycles, the characteristic peaks of

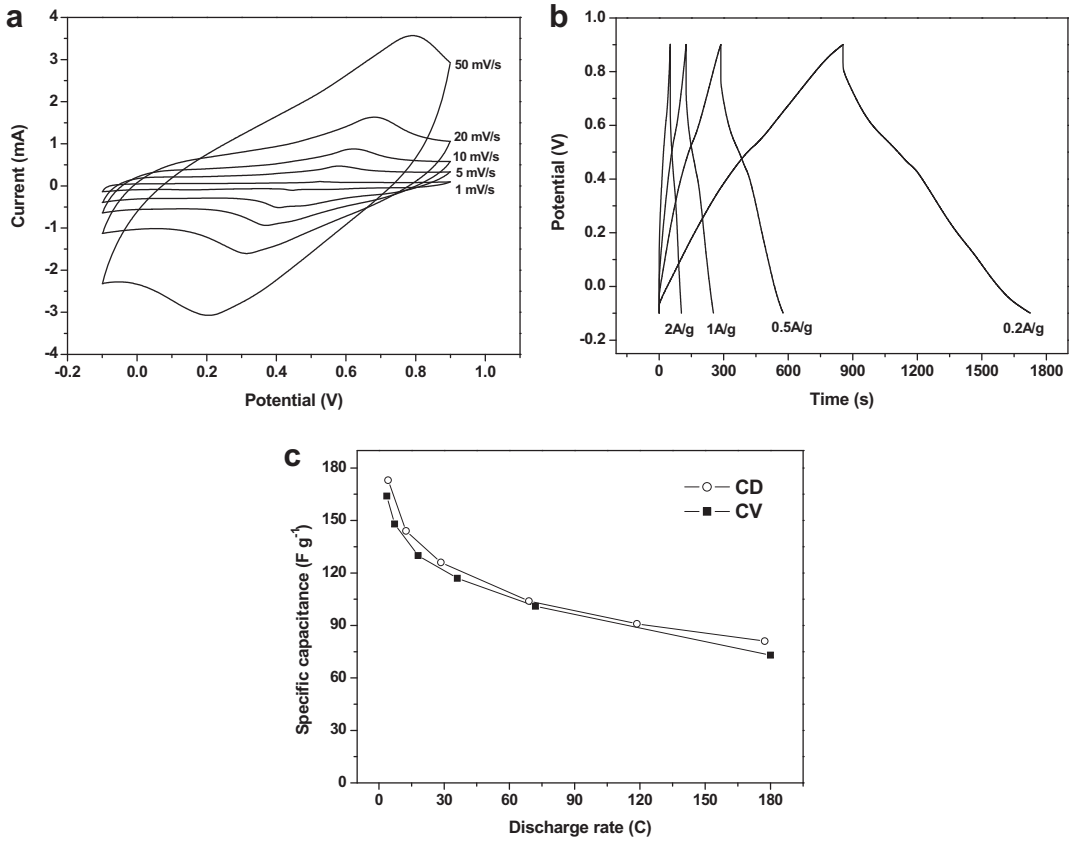

Fig. 9. (a) Cyclic voltammograms at various scan rates and (b) Charge–discharge curves at different current densities for the Mg–buserite electrode after 500 cycles. (c) The corresponding specific capacitance as a function of discharge rate.

Mg–buserite at $2\theta = 9.1°$, 18.3° and 27.5° are still remained, except that the diffraction intensity of these peaks decreased. This result reflects that long-term electrochemical cycling does not induce significant structural modifications of Mg–buserite.

For the purpose of understanding the difference in the chemical bonds present in Mg–buserite before and after 500 cycles, FT-IR analysis was carried out in the wavelength range from 450 to 4000 cm^{-1}. As shown in Fig. 10, it can be observed that the FT-IR spectrum of the Mg–buserite after 500 cycles (Fig. 10b) displays similar features as that of the sample before cycle (Fig. 10a). The two spectra show the broad bands at approximately 3430 cm^{-1}, which should be attributed to the O–H stretching vibrations of hydroxyl groups or adsorbed water molecules [37]; the absorption peaks at around 1634, 1385 and 1186 cm^{-1} can be assigned to the O–H bending vibrations combined with Mn atoms [20,36]; the absorption peaks at approximately 746, 514 and 484 cm^{-1} can be observed in the two spectra, which are normally attributed to the Mn–O stretching vibrations in MnO_6 octahedra framework [38]. The FT-IR results combine with the above XRD results demonstrate the excellent structural and microstructural stability of the Mg–buserite electrode during electrochemical cycling.

The long-term cycling stability of Mg–buserite was examined by a large number of CV cycles up to 22,000 cycles. The variation of the specific capacitance as a function of cycle number is shown in Fig. 11(a). The specific capacitance of the Mg–buserite electrode sharply increases during the initial 500 cycles and reaches the maximum at approximately the 500th cycle, and then it remains an almost constant value and decreases slightly upon prolonged cycling. After 22,000 cycles, the specific capacitance decreases by approximately 6% of the maximum specific capacitance. The result is much better than the previous report of birnessite [12], in which the specific capacitance decreases by 16% of the initial capacitance after 1800 cycles. The cycle life of the as-prepared Mg-doped Na–birnessite was also investigated in the same experimental condition, and the variation of the specific capacitance over 6000 cycles is given in Fig. 11(b). The specific capacitance of the Mg-doped Na–birnessite electrode decreases by approximately 15% of its maximum specific capacitance only after 6000 cycles. The experimental results demonstrate that the cycling stability of Mg–buserite is more excellent than that of birnessite, and further suggest that Mg–buserite is a promising electrode material for supercapacitor applications.

According to previous literature, two mechanisms were proposed to explain the charge storage behavior of manganese dioxide as an electrode material for supercapacitors in mild solutions. The first is the surface adsorption of electrolyte cations ($C^+ = H^+$, Li^+, Na^+ or K^+) on the manganese oxides [39].

$$(MnO_2)_{surface} + C^+ + e^- \leftrightarrow \left(MnO_2{}^-C^+\right)_{surface} \quad (3)$$

The second is based on the intercalation or deintercalation of electrolyte cations ($C^+ = H^+$, Li^+, Na^+ or K^+) in the bulk of the manganese oxides during reduction [40].

$$MnO_2 + C^+ + e^- \leftrightarrow MnOOC^+ \quad (4)$$

On the basis of the above experimental results and charge storage mechanisms of MnO_2, the charge storage behaviors of the Mg–buserite electrode during cycles are clear. At first, the initial specific capacitance of the Mg–buserite electrode is mainly due to the surface adsorption of electrolyte cations, accompanied by the valence conversion of Mn^{4+}/Mn^{3+}, as described in Eq. (3). Then, the specific capacitance sharply increased during the initial 500 cycles, which is attributed to an electrochemical activation process [33]. During the initial electrochemical cycles, the electric force can allow the co-intercalation of electrolyte ions and solvent into the small pore structure of the Mg–buserite electrode where the electrolyte ions cannot be present without an electrochemical polarization [41,42]. As a result, the electrochemically activated Mg–buserite provides more active points and favorable pathways for the intercalation/deintercalation of electrolyte cations. According to Eq. (4), larger amount of Na^+ ions reversibly intercalate/deintercalate in the bulk of the Mg–buserite electrode, also accompanied by change of the manganese oxidation state, providing more pseudocapacitive contribution. Thus, the Mg–buserite electrode exhibits excellent capacitance behavior after 500 cycles. The specific capacitance of the Mg–buserite electrode remains an almost constant value and decreases slightly upon prolonged cycling up to 22,000 cycles, indicating that the structure of the Mg–buserite are maintained even after 22,000 cycles [43]. This is because the diameter of the hydration shell of the Mg^{2+} ion is larger than that of the Na^+ ion, the intercalation and deintercalation of Na^+ ions into the interlayer of the Mg–buserite does not result in significant structural changes.

The electrochemical properties of the Mg–buserite electrode before and after cycles were also studied by EIS, and Nyquist plots at different potentials are shown in Fig. 12a. All of the measured impedance plots are similar in shape, which composed of

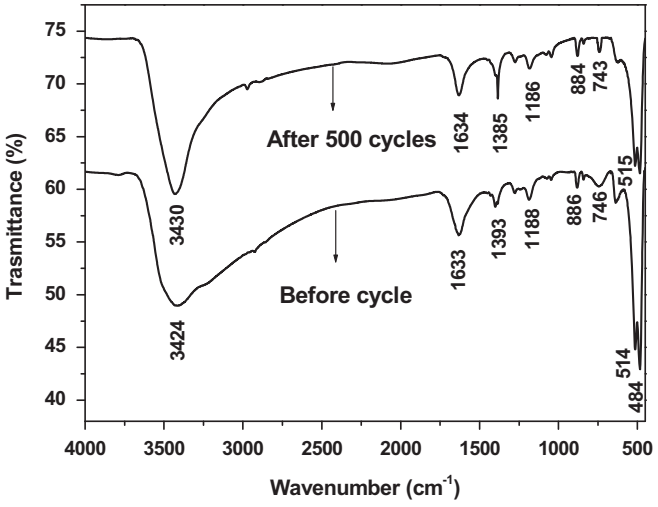

Fig. 10. FT-IR spectra of Mg–buserite: (a) before and (b) after 500 cycles.

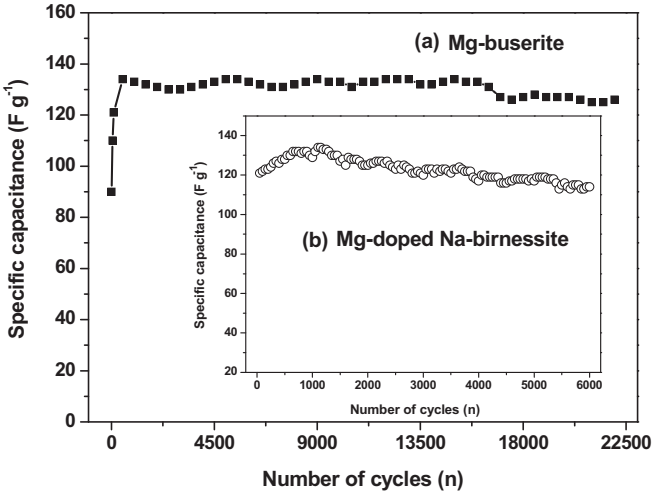

Fig. 11. Variations of the specific capacitance with respect to cycle number for (a) Mg–buserite and (b) Mg-doped Na–birnessite electrodes.

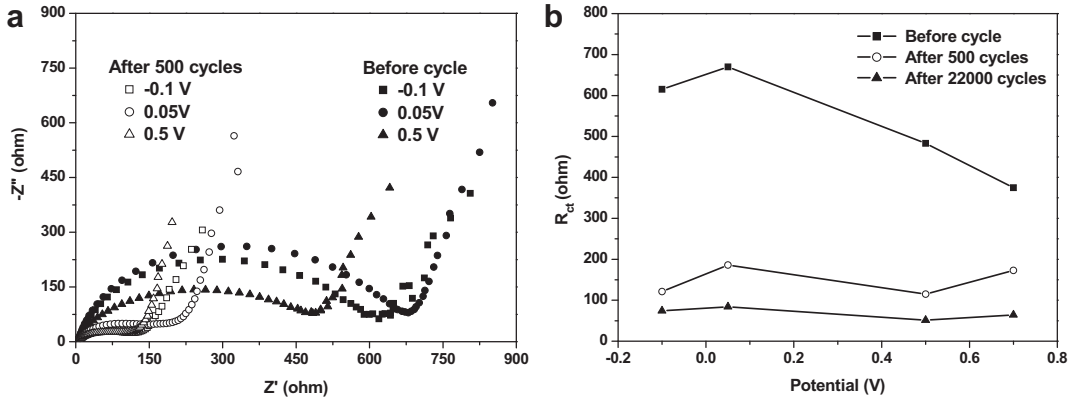

Fig. 12. (a) Nyquist plots of the Mg–buserite electrode in the frequency range of 10^{-2} Hz–100 kHz: before and after 500 cycles. (b) The charge-transfer resistance (R_{ct}) as a function of the potential of the Mg–buserite electrode after various cycling numbers.

a semicircle at the high frequencies region, following by a relative straight slopping line at the low frequencies region. At very high frequencies, the intercepts at real part Z′ are almost the same, which means that all of the EIS curves exhibit the same combination resistance of the intrinsic resistance of the Mg–buserite, the ionic resistance of the electrolyte and the contact resistance at the interface between Mg–buserite and current collector [44]. The semicircle in the high-frequency range is usually associated with the surface properties of the electrode, and the diameter of the semicircle corresponds to the charge-transfer resistance (R_{ct}) of the electrode, which is called the Faraday resistance [45]. It can be easily observed from Fig. 12a that the diameters of the semicircles clearly decrease after 500 cycles. The diameters of the semicircles decrease during the initial cycling have already been reported by Qu et al. [46]. At lower frequencies, the straight sloping lines along the imaginary axis represent the diffusive resistance of the electrolyte in the electrode pores [47].

Variations in the R_{ct} of the Mg–buserite electrode before cycle, after 500 cycles and after 22,000 cycles with the potential are shown in Fig. 12b. All of the R_{ct} of the Mg–buserite electrode before cycle at various potentials are very large, but after 500 cycles, the R_{ct} are reduced obviously. Thereafter, the R_{ct} at different potentials reduces slightly after 22,000 cycles. It can be concluded that the initial several cycles is an activation process, which leads to a decreased charge-transfer resistance which contributed to the increase in the specific capacitance [11].

4. Conclusions

In this paper, a hydration-layered Mg–buserite for supercapacitor applications was successfully synthesized. The as-prepared Mg–buserite has a large basal spacing of 10 Å and possesses Mg^{2+} ions and two sheets of water molecules in the interlayer region. The electrochemical performances of the synthesized material were evaluated by CV, CD and EIS experiments. The experimental results showed that the specific capacitance of the Mg–buserite electrode sharply increased during the initial 500 cycles and reached a maximum of 164 F g^{-1} at approximately the 500th cycle at a scan rate of 1 mV s^{-1}. The increase in the specific capacitance of the Mg–buserite electrode during the initial 500 cycles is attributed to an electrochemical activation process, which is driven by an electric force. The electric force can allow the co-intercalation of electrolyte ions and solvent into the small pore structure of the Mg–buserite electrode, which provides more active points and favorable pathways for the intercalation/deintercalation of electrolyte ions, and produce more pseudocapacitive contribution. Thereafter, the specific capacitance remained an almost constant value and decreased slightly upon prolonged cycling. After 22,000 cycles, the specific capacitance decreased by approximately 6% of the maximum specific capacitance. Because the hydrated Mg^{2+} ion is larger than the hydrated Na^{+} ion, the intercalation and deintercalation of Na^{+} ions from the electrolyte into the interlayer of Mg–buserite do not induce the significant structural or microstructural changes. Thus, the as-prepared Mg–buserite exhibits superior capacitive behavior and excellent cycling stability. The above analysis results demonstrate that the as-prepared Mg–buserite is a promising candidate as an electrode material for supercapacitors.

Acknowledgments

The authors wish to acknowledge the financial support for this work from the project of Guangdong Province Science and Technology Bureau (Grant No. 2010B090400552), Natural Science Foundation of Guangdong Province, China (Grant No. S2011010003416), Project of Guangzhou Science and Information Technology Bureau (Grant No. 12A42091603) and National Natural Science Foundation of China (Grant No. 20877025).

References

[1] B.E. Conway, Electrochemical Supercapacitors, Scientific Fundamentals and Technological Applications, Kluwer Academic/Plenum Press, New York, 1999.
[2] R.N. Reddy, R.G. Reddy, J. Power Sources 132 (2004) 315–320.
[3] J.R. Miller, A.F. Burke, Electrochem. Soc. Interface Spring 17 (2008) 53–57.
[4] L.L. Zhang, X.S. Zhao, Chem. Soc. Rev. 38 (2009) 2520–2531.
[5] E. Beaudrouet, A.L.G.L. Salle, D. Guyomard, Electrochim. Acta 54 (2009) 1240–1248.
[6] S. Sarangapani, B.V. Tilak, C.P. Chen, J. Electrochem. Soc. 143 (1996) 3791–3799.
[7] J.P. Zheng, T.R. Jow, J. Power Sources 62 (1996) 155–159.
[8] X.L. Wang, A.B. Yuan, Y.Q. Wang, J. Power Sources 172 (2007) 1007–1011.
[9] L. Athouel, F. Moser, R. Dugas, O. Crosnier, D. Belanger, T. Brousse, J. Phys. Chem. C 112 (2008) 7270–7277.
[10] Y. Matsuo, Y. Miyamoto, T. Fukutsuka, Y. Sugie, J. Power Sources 146 (2005) 300–303.
[11] A. Ogata, S. Komaba, R. Baddour-Hadjean, J.P. Pereira-Ramos, N. Kumagai, Electrochim. Acta 53 (2008) 3084–3093.
[12] S. Komaba, T. Tsuchikawa, A. Ogata, N. Yabuuchi, D. Nakagawa, M. Tomita, Electrochim. Acta 59 (2012) 455–463.
[13] Q.M. Gao, O. Giraldo, W. Tong, S.L. Suib, Chem. Mater. 13 (2001) 778–786.
[14] G.B. Lei, Mar. Geol. 133 (1996) 103–112.
[15] S. Ching, K.S. Krukowska, S.L. Suib, Inorg. Chim. Acta 294 (1999) 123–132.
[16] X. Yang, H. Kanoh, W. Tang, Z. Liu, K. Ooi, Chem. Lett. (2001) 612–613.
[17] J. Luo, Q.H. Zhang, A.M. Huang, O. Giraldo, S.L. Suib, Inorg. Chem. 38 (1999) 6106–6113.
[18] Q. Feng, K. Yanagisawa, N. Yamasaki, Chem. Commun. 14 (1996) 1607–1608.
[19] D.C. Golden, C.C. Chen, J.B. Dixon, Science 231 (1986) 717–719.

[20] T. Gao, M. Glerup, F. Krumeich, R. Nesper, H. Fjellvag, P. Norby, J. Phys. Chem. C 112 (2008) 13134–13140.
[21] J.P. Zheng, P.J. Cygan, T.R. Jow, J. Electrochem. Soc. 142 (1995) 2699–2703.
[22] A. Yuan, Q.L. Zhang, Electrochem. Commun. 8 (2006) 1173–1178.
[23] S. Devaraj, N. Munichandraiah, J. Electrochem. Soc. 154 (2007) A80–A88.
[24] M. Kruk, M. Jaroniec, Chem. Mater. 13 (2001) 3169–3183.
[25] M.W. Xu, L.B. Kong, W.J. Zhou, H.L. Li, J. Phys. Chem. C 111 (2007) 19141–19147.
[26] S.L. Chou, F.Y. Cheng, J. Chen, J. Power Sources 162 (2006) 727–734.
[27] J.K. Chang, C.H. Huang, M.T. Lee, W.T. Tsai, M.J. Deng, I.W. Sun, Electrochim. Acta 54 (2009) 3278–3284.
[28] M. Chigane, M. Ishikawa, M. Izaki, J. Electrochem. Soc. 148 (2001) D96–D101.
[29] M. Chigane, M. Ishikawa, J. Electrochem. Soc. 147 (2000) 2246–2251.
[30] B. Djurfors, J.N. Broughton, M.J. Brett, D.G. Ivey, Acta Mater. 53 (2005) 957–965.
[31] S.W. Donne, A.F. Hollenkamp, B.C. Jones, J. Power Sources 195 (2010) 367–373.
[32] H.S. Nam, J.S. Kwon, K.M. Kim, J.M. Ko, J.D. Kim, Electrochim. Acta 55 (2010) 7443–7446.
[33] Z.J. Sun, H.Y. Chen, D. Shu, C. He, S.Q. Tang, J. Zhang, J. Power Sources 203 (2012) 233–242.
[34] M.W. Xua, W. Jia, S.J. Bao, Z. Su, B. Dong, Electrochim. Acta 55 (2010) 5117–5122.
[35] V. Subramanian, H.W. Zhu, R. Vajtai, P.M. Ajayan, B.Q. Wei, J. Phys. Chem. B 109 (2005) 20207–20214.
[36] A.B. Yuan, X.L. Wang, Y.Q. Wang, J. Hu, Electrochim. Acta 54 (2009) 1021–1026.
[37] Z. Liu, X. Yang, Y. Makita, K. Ooi, Chem. Mater. 14 (2002) 4800–4806.
[38] M.V. Ananth, S. Pethkar, K. Dakshinamurthi, J. Power Sources 75 (1998) 278–282.
[39] H.Y. Lee, J.B. Goodenough, J. Solid State Chem. 144 (1999) 220–223.
[40] M. Toupin, T. Brousse, D. Belanger, Chem. Mater. 16 (2004) 3184–3190.
[41] S. Mitani, S.I. Lee, K. Saito, Y. Korai, I. Mochida, Electrochim. Acta 51 (2006) 5487–5493.
[42] T. Ohta, I.T. Kim, M. Egashira, N. Yoshimoto, M. Morita, J. Power Sources 198 (2012) 408–415.
[43] J.Q. Yuan, Z.H. Liu, S.F. Qiao, X.R. Ma, N.C. Xu, J. Power Sources 189 (2009) 1278–1283.
[44] J. Gamby, P.L. Taberna, P. Simon, J.F. Fauvarque, M. Chesneau, J. Power Sources 101 (2001) 109–116.
[45] W. Xiao, H. Xia, J.Y.H. Fuh, L. Lu, J. Power Sources 193 (2009) 935–938.
[46] Q.T. Qu, P. Zhang, B. Wang, Y.H. Chen, S. Tian, Y.P. Wu, R. Holze, J. Phys. Chem. C 113 (2009) 14020–14027.
[47] C. Lin, J.A. Ritter, B.N. Popov, J. Electrochem. Soc. 145 (1998) 4097–4103.